

Rubbing Against Blood Clots using Helical Robots: Modeling and *In Vitro* Experimental Validation

Islam S. M. Khalil*, Ahmet Fatih Tabak†, Khaled Sadek*, Dalia Mahdy*, Nabila Hamdi*, and Metin Sitti†

Abstract—The risk of side-effects from thrombolytic agents can be minimized by using smaller doses, assisted by mechanical rubbing against blood clots using helical robots. Quantifying this observation, we study the influence of rubbing against clots on their removal rate *in vitro*. First, we present a hydrodynamic model of the helical robot based on resistive-force theory to investigate the rubbing behaviour of the clots using robot driven by two rotating dipole fields. Second, we experimentally evaluate the influence of the rubbing on the removal rate of the blood clots. Not only do we find that the removal rate of rubbing ($-0.56 \pm 0.27 \text{ mm}^3/\text{min}$) is approximately 3 times greater than the dissolution rate of chemical lysis using streptokinase ($-0.17 \pm 0.032 \text{ mm}^3/\text{min}$), but we also show that this removal rate can be controlled via the rubbing speed of the robot.

I. INTRODUCTION

Over the past decade, external actuation of man-made robots at the nano- and micro-scales have shown potential to revolutionize medicine and technology [1], [2], [3]. It is possible to direct and/or drive these robots via the action of a magnetic field without the need of onboard power supply and onboard control system. At this scale, the domination of the viscous forces suppresses the hydrodynamic inertial forces which necessitates nonreciprocal periodic changes in the shape of the robot to break time-reversal symmetry [4]. Helical propulsion has long been employed to break time-reversal symmetry and provide locomotion [5], [6] in low-Reynolds number fluids and to drill through tissue [7], [8] via the action of a uniform or a non-uniform rotating magnetic field. The versatility of helical propulsion (and magnetic actuation in general) has proven to be useful in a wide range of nanotechnology and biomedical applications [1]. Locomotion in three-dimensional space [9], high-precision transportation and carrying cargos [10], microassembly [11], targeting and transportation of biological cells [12], propulsion of nanomotors inside HeLa cervical cancer cells [13], and *in vitro* targeted drug delivery [14] have been demonstrated using the mentioned approach. Very recently, Servant *et al.* [15] have achieved magnetically controlled navigation of a swarm of artificial bacterial flagella in the peritoneal cavity of a mouse *in vivo*. Medina *et al.* have used helical propulsion to assist immotile sperm cells to achieve *in vitro* fertilization [16]. In addition, Ullrich *et al.* have investigated the swimming

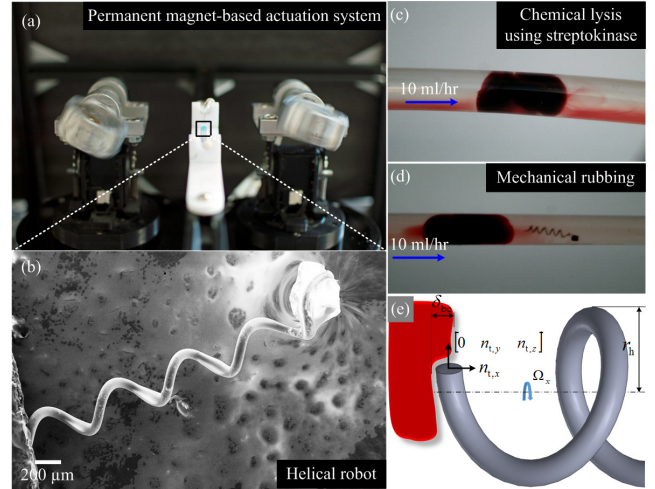


Fig. 1. A permanent magnet-based actuation system with a helical tail-based magnetic robot is used to generate rotating magnetic fields and achieve mechanical rubbing of blood clots. (a) The clot is contained inside a catheter segment and positioned between two rotating permanent magnets. (b) Scanning electron microscopy image of a helical robot shows its helical tail and magnetic head. (c and d) Experiments are conducted on two groups, i.e., chemical lysis using streptokinase and pure rubbing against the clot. (e) The robot rotates at frequency Ω_x , and $\delta_{b,c}$ represents the incremental change in the volume of the clot. $n_{t,y}(t)$ and $n_{t,z}(t)$ are the components of the surface normal at the rotating tip of the tail in the frame of the robot. $n_{t,x}(t)$ indicates the direction of rubbing against the clot.

performance of helical robots in fibrous environments with various collagen fibre concentrations [17]. It follows from the mentioned proof-of-concept studies that several research groups are exerting expanded efforts to operate robots inside *in vivo* environments for biomedical applications. In this work, we expand on our previous proof-of-concept study [18] and achieve the following: (1) Modeling of the fretting behaviour due to rubbing against the blood clots using helical robots. (2) Rubbing of the blood clots *in vitro* and characterization of the optimal rubbing frequency. (3) Comparative study between chemical lysis using a thrombolytic agent and mechanical rubbing with the robot. First, the motion of the robot under the influence of two synchronized rotating magnetic fields is studied by developing a hydrodynamic model based on resistive-force theory (RFT). This model describes the locomotion of the robot in low-Reynolds number and the rubbing behaviour against blood clots inside catheter segments, as shown in Fig. 1. Second, we control the motion of the robot inside the segments towards blood clots and compare the removal rate of the rubbing to dissolution

*The authors are affiliated with the German University in Cairo, Egypt.

†The authors are affiliated with the Physical Intelligence Department, Max Planck Institute for Intelligent Systems, Stuttgart, Germany.

This work was supported by funds from the German University in Cairo and the DAAD-BMBF funding project. The authors also acknowledge the funding from the Science and Technology Development Fund in Egypt (No. 23016).

rate of lysis using a thrombolytic agent (streptokinase), and investigate the optimal rubbing frequency to achieve maximum removal rate of the clot. The remainder of this paper is organized as follows: Section II provides modeling of the propulsion and the rubbing behaviour against blood clot. The influence of the lysis and rubbing on the removal of blood clots is experimentally investigated in Section III. Finally, Section IV concludes and provides directions for future work.

II. RUBBING AGAINST BLOOD CLOTS

The actuation mechanism of the helical robots is based on two rotating permanent magnets placed parallel to a cylindrical catheter segment (Fig. 2) [19]. This segment contains the robot, and is filled with a medium (phosphate buffered saline) with higher viscosity than blood to approach the low Reynolds numbers ($< 10^{-2}$) achieved by microrobots. We calculate the corresponding field and field gradient based on the analysis presented by Petruska and Abbott [20] and Rakotoarison *et al.* [21], and formulate scalar potential for the rotating cylindrical magnets, $\Phi_m(\mathbf{r}, \theta, z)$. Using the assumptions of azimuthal symmetry, i.e., $\theta=0$, and uniform polarization with respect to radial position, the potential is approximated at the position of the robot (\mathbf{r}) as follows:

$$\Phi_m(\mathbf{r}, \theta, z) = \frac{1}{4\pi} \int_V \frac{\nabla \cdot \mathbf{M}}{|\mathbf{r} - \rho|} dV, \quad (1)$$

where \mathbf{M} is the magnetization vector of the permanent magnet, ρ is a position vector to be integrated over the volume of the permanent magnet, and dV signifies the infinitesimal increment in the volume. The gradient of $\Phi_m(\mathbf{r}, \theta, z)$ provides the following magnetic field density (\mathbf{B}):

$$\mathbf{B} = -\mu_0 \nabla \Phi_m(\mathbf{r}, \theta, z), \quad (2)$$

where μ_0 is the permeability of free space. Once the magnetic field (\mathbf{B}) is calculated for the two permanent magnets, the magnetic force (\mathbf{F}_m) and magnetic torque (\mathbf{T}_m) exerted on the robot are calculated using

$$\begin{pmatrix} \mathbf{F}_m \\ \mathbf{T}_m \end{pmatrix} = \begin{pmatrix} (\mathbf{m} \cdot \nabla)(\mathbf{R}_1 \mathbf{B}_1 + \mathbf{R}_2 \mathbf{B}_2) \\ \mathbf{m} \times (\mathbf{R}_1 \mathbf{B}_1 + \mathbf{R}_2 \mathbf{B}_2) \end{pmatrix}. \quad (3)$$

In (3), \mathbf{m} is the total magnetization vector of the robot, and \mathbf{R}_1 and \mathbf{R}_2 are the rotation matrices from frames of the first and second permanent magnets to the frame of the robot, respectively. Further, \mathbf{B}_1 and \mathbf{B}_2 are the magnetic fields of the first and second permanent magnets, respectively. The configuration of the rotating permanent magnets (Fig. 2) enables us to apply pure magnetic torque on the robot (when the robot is located at the common centers of the rotating permanent magnets along x -axis) [19]. Any deviation in the position of the robot along x -axis will result in a magnetic force that will contribute to the propulsion force. We calculate the Reynolds number as $Re = \frac{\rho |\mathbf{v}| L}{\mu} = 0.089$, where ρ is the density of the fluid (995 kg.m^{-3}), \mathbf{v} is the velocity of the robot before rubbing ($20 \times 10^{-3} \text{ m.s}^{-1}$) and L is its length ($4 \times 10^{-3} \text{ m}$), and μ is the dynamic viscosity of the fluid (0.8882 Pa.s). The calculated Reynolds number

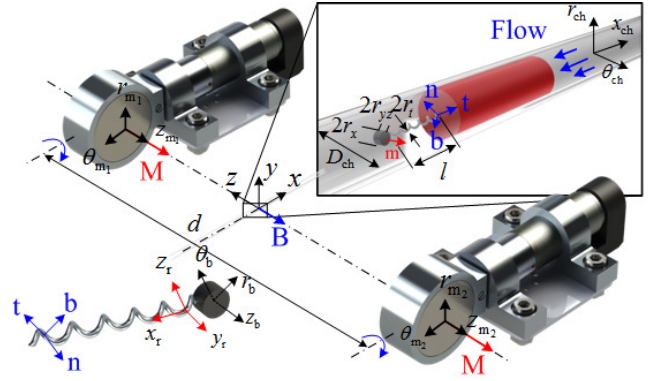


Fig. 2. The helical robot (inset) is contained inside a catheter (diameter D_{ch}) segment between two rotating permanent magnets (magnetization \mathbf{M}). Rotation of the permanent magnets generates a rotating field (\mathbf{B}) that exerts a magnetic torque on the dipole of the robot (\mathbf{m}). The robot consists of a cylindrical NdFeB magnet with diameter r_x , height r_{yz} , and tail length l .

represents an upper-limit since the speed of the robot during rubbing is on the order of $\mathcal{O}(10^{-4}) \text{ m.s}^{-1}$. This speed results in a Reynolds number of 0.004. Therefore, motion of the robot is governed by

$$\begin{pmatrix} \mathbf{F}_m + \mathbf{F}_g + \mathbf{F}_d + \mathbf{F}_c + \mathbf{F}_f \\ \mathbf{T}_m + \mathbf{T}_g + \mathbf{T}_d + \mathbf{T}_c + \mathbf{T}_f \end{pmatrix} = 0, \quad (4)$$

where \mathbf{F}_d and \mathbf{T}_d denote the viscous drag force and torque vectors, respectively. \mathbf{F}_f and \mathbf{T}_f are the fretting force and fretting torque due to the rubbing action between the robot and the clot (as shown in Fig. 1(c)), respectively. \mathbf{F}_c and \mathbf{T}_c denote the reaction force and torque when the head or the tail of the robot are in contact with the channel boundary. Further, \mathbf{F}_g and \mathbf{T}_g are the force and torque exerted on the robot due to gravity, and are given by

$$\begin{pmatrix} \mathbf{F}_g \\ \mathbf{T}_g \end{pmatrix} = \begin{pmatrix} V(\rho_r - \rho_f) \mathbf{R}_{Lab}^T \mathbf{g} \\ (\mathbf{r}_{cov} - \mathbf{r}_{com}) \times \mathbf{F}_g \end{pmatrix}, \quad (5)$$

where \mathbf{g} is a vector signifying gravitational attraction and \mathbf{R}_{Lab} is the time-dependent rotation matrix between the robot and a fixed frame of reference. ρ_r and ρ_f are the density of the robot and density of the medium, respectively. Further, \mathbf{r}_{cov} and \mathbf{r}_{com} are the center of volume and center of mass of the robot, respectively. The viscous drag on the magnetic robot is calculated based on RFT, by incorporating the wall effects on the tail and head [22], [23], and the complex hydrodynamic interactions [24] as:

$$\begin{pmatrix} \mathbf{F}_d \\ \mathbf{T}_d \end{pmatrix} = \left(\int_l \begin{bmatrix} \mathbf{R} \mathbf{C} \mathbf{R}^T & -\mathbf{R} \mathbf{C} \mathbf{R}^T \mathbf{S} \\ \mathbf{S} \mathbf{R} \mathbf{C} \mathbf{R}^T & -\mathbf{S} \mathbf{R} \mathbf{C} \mathbf{R}^T \mathbf{S} \end{bmatrix} dl \right. \\ \left. + \begin{bmatrix} \mathbf{R}_{ch} \mathbf{D} \mathbf{R}_{ch}^T & -\mathbf{R}_{ch} \mathbf{D} \mathbf{R}_{ch}^T \mathbf{S} \\ \mathbf{S} \mathbf{R}_{ch} \mathbf{D} \mathbf{R}_{ch}^T & \mathbf{E} \end{bmatrix} \right) \begin{pmatrix} \mathbf{U} + \mathbf{U}_{ch} \\ \Omega \end{pmatrix}, \quad (6)$$

where l is the length of the tail. \mathbf{U} and Ω are the rigid-body linear and angular swimming velocity vectors of the robot, respectively. \mathbf{U}_{ch} is the flow vector inside the channel and \mathbf{R} is the rotation matrix between local Frenet-Serret frames and the reference frame of the robot [25]. In addition, \mathbf{R}_{ch}

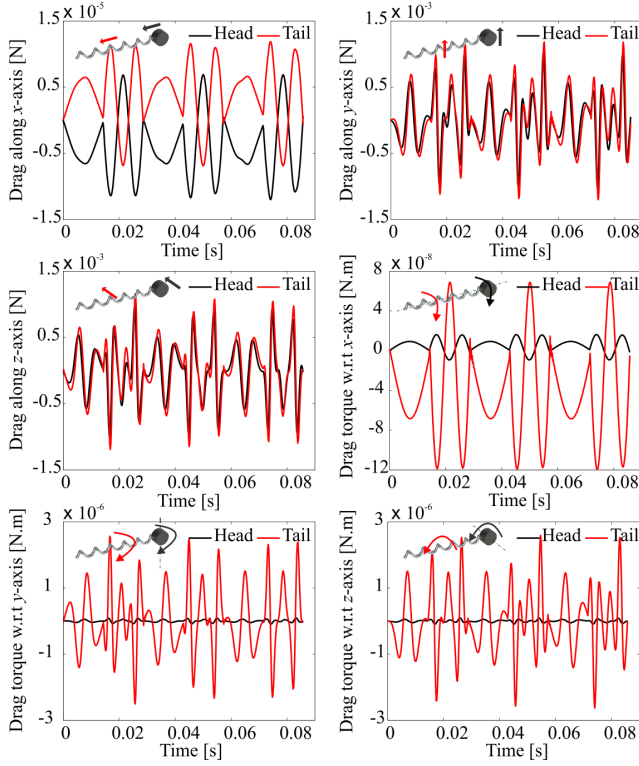


Fig. 3. Simulation results of the drag forces and torques (using (6)) exerted on the head and the helical tail of the robot, at frequency of 35 Hz.

is a projection matrix of the cylindrical coordinates of the channel to the Cartesian coordinates residing on the center of mass of the robot, and \mathbf{S} signifies local cross products. The hydrodynamic forces, i.e., propulsive and resistive drag acting on the moving surfaces, are given by the resistance matrices, \mathbf{C} , \mathbf{D} , and \mathbf{E} . Matrix \mathbf{C} is calculated for the tail as, $\mathbf{C} = \text{diag}(c_t, c_n, c_b)$, where c_t , c_n , and c_b are the local resistance coefficients along the Frenet-Serret frames of the tail and are articulated by Brennen and Winet [22]. Matrix \mathbf{D} provides the fluid resistance coefficients of the magnetic head for the translational rigid-body motion as follows:

$$\mathbf{D} = \begin{pmatrix} \Upsilon_x D_x & 0 & 0 \\ 0 & \Upsilon_{r\theta} D_r \cos \phi & \Upsilon_{r\theta} D_r \sin \phi \\ 0 & \Upsilon_{r\theta} D_\theta \sin \phi & \Upsilon_{r\theta} D_\theta \cos \phi \end{pmatrix}. \quad (7)$$

Here D_x , D_r , and D_θ are provided by Higdon and Muldowney [23] using lubrication theory, and the complex hydrodynamic interaction terms, i.e., Υ_x , $\Upsilon_{r\theta}$, and ϕ , are articulated by Tabak and Yesilyurt [24]. These coefficients are used to predict the hydrodynamic interaction between moving and stationary surfaces. Finally, \mathbf{E} provides the fluid resistance coefficients of the head for the rotational rigid-body motion as follows:

$$\mathbf{E} = -\text{diag}(8\zeta_x \pi \mu r_x r_{yz}^2, 8\zeta_y \pi \mu r_x r_{yz}^2, 8\zeta_z \pi \mu r_x r_{yz}^2), \quad (8)$$

where μ is the dynamic viscosity of the medium, and r_x and r_{yz} are the radius of the magnetic head and its height, respectively. Further, ζ_i , for $i = x, y, z$, are numerical tuning coefficients to compensate for geometric aberrations. Fig. 3

provides the drag forces and torques exerted on the head and tail of the robot. The total drag force on head and tail, along x -axis, cancel each other during free swimming as there is no other significant force along x -axis. On the other hand, the drag torque on the head and tail, along x -axis, do not balance each other because of the presence of magnetic torque. Similarly, one can deduce the importance of other physical stimuli by inspecting the pure drag force and drag torque balance on all axes. The wall contact is given by a series of equations based on a penalty method for the following hypothetical scenario [26]:

$$\begin{pmatrix} \mathbf{F}_c \\ \mathbf{T}_c \end{pmatrix} = \begin{pmatrix} k \begin{cases} \delta, & \text{if } \delta \leq 0 \\ 0, & \delta > 0 \end{cases} + b \begin{cases} \frac{d\delta}{dt}, & \text{if } \frac{d\delta}{dt} > 0 \\ 0, & \frac{d\delta}{dt} \leq 0 \end{cases} \\ \mathbf{r}_c \times \mathbf{F}_c \end{pmatrix} \mathbf{n}_c, \quad (9)$$

where δ is the penetration depth along the radial direction, w is a weighing function to enable the realization of an over-damped system condition to prevent oscillations ($0 \leq w \leq 1$). Further, \mathbf{n}_c is the surface normal of the channel wall at the point of contact, and \mathbf{r}_c is the position vector of the contact point on the surface of the magnetic robot. In (9), k and b are given by

$$k = \frac{w |\mathbf{F}_c|}{\delta} \quad \text{and} \quad b = \frac{(1-w) |\mathbf{F}_c|}{|\frac{d\delta}{dt}|}. \quad (10)$$

Furthermore, (10) includes the reaction force of the channel walls using a spring-damper model, and allows damping effect only for positive velocities, while avoiding sticky surface condition for negative velocities and non-zero δ larger than a predefined value of $\delta \geq 10^{-6} r_{yz}$. $|\mathbf{F}_c|$ is calculated by adding the hydrodynamic, magnetic, and forces due to gravity along the surface normal on the wall at the point of contact [26], and by solving (4). In order to obtain the velocities and the position vector relative to a fixed frame of reference we use, $[\mathbf{U}_{\text{Lab}} \quad \boldsymbol{\Omega}_{\text{Lab}}]^T = \mathbf{R}_{\text{Lab}} [\mathbf{U} \quad \boldsymbol{\Omega}]^T$. The rotation matrix \mathbf{R}_{Lab} is obtained by quaternion calculations [29] as the robot experiences complex rigid-body rotations. Position vector along the cylindrical channel and rigid-body rotation matrix (\mathbf{R}_{Lab}) are obtained by simple Forward-Euler integration over time.

From this point onwards we focus on the fretting force and torque using conservation of energy and momentum. The rubbing against (Fig. 1(e)) the blood clot, δ_{bc} , is calculated based on torque equilibrium between the fretting torque and the difference between external magnetic torque and drag torque exerted on the helical robot using dimensional analysis. The fretting of material in volume requires certain amount of power which is harnessed from the rotation of the tail with a net torque that is approximated by

$$(|T_{m,x}| - |T_{d,x}|) \Omega_x \approx 0.25 \tau \pi \Omega_x \delta_{bc}^2, \quad (11)$$

where $T_{m,x}$ and $T_{d,x}$ are the magnetic and efficient drag torque of the rest of the physical stimuli acting on the robot with respect to x -axis of the robot, respectively. τ is the ultimate-tensile strength of the blood clot [30]. It is possible to approximate δ_{bc} based on the assumption that the removal

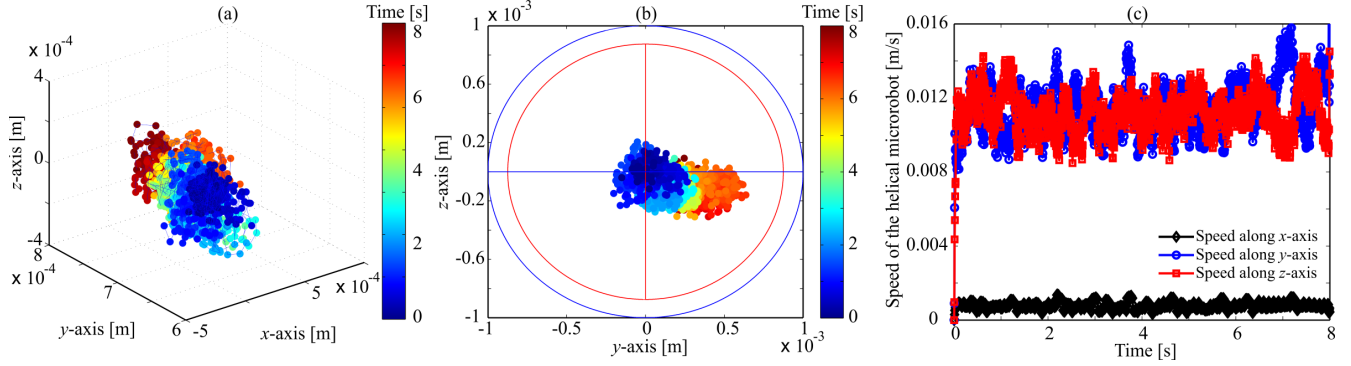


Fig. 4. Rubbing behavior of a helical robot against a blood clot for $t \in [0, 8]$. (a) The evolution of the position of the robot is plotted at equal time intervals over 75 cycles. (b) The robot drifts towards the channel wall while rubbing against the clot. The blue circle represents the inner-diameter of the catheter segment, whereas the red circle represents a position limit on the robot. (c) Motion of the robot along x -axis is constrained by the clot during rubbing, whereas oscillations are observed along y - and z -axis. The removal rate of clot in this simulation is $-0.834 \text{ mm}^3/\text{min}$, at frequency of 35 Hz.

rate is relatively small, and the helix removes the material in small fragments during its rotation with respect to x -axis of the robot. Based on the principle of conservation of momentum, the work done by the tip of the rotating tail is equal to the work done by the removed material. Under the assumptions that the removed material with infinitesimal volume is cylindrical in shape, and the fracture strength is the maximum measured ultimate tensile strength, we can approximate δ_{bc} using

$$\delta_{bc} = \begin{cases} \min\left(\frac{2\sqrt{|\mathbf{T}_{m,x}| - |\mathbf{T}_{d,x}|}}{\sqrt{\pi r r_h}}, 0.5r_t\right), & \text{if } x_{bc} < r_{xtip} \\ 0, & x_{bc} \geq r_{xtip} \end{cases} \quad (12)$$

where r_h and r_t are the radii of the helix and tail, respectively. Further, x_{bc} and r_{xtip} denote the position of the blood clot and position of the tip of the tail, respectively, along x -axis of the channel (x_{ch}). The conservation of energy in terms of work done on small volumes of soft-tissue is used for modeling and characterization of local cutting and puncturing as presented in [31] and [32], as opposed to finite element analysis used to compute soft-tissue behavior under fracture conditions [33]. This penetration depth prediction leads to the following fretting force and torque on the robot:

$$\begin{pmatrix} f_{f,x} \\ f_{f,y} \\ f_{f,z} \end{pmatrix} = \begin{pmatrix} \left(k_{bc}\delta_{bc} + b_{bc} \begin{cases} \frac{d\delta_{bc}}{dt}, & \text{if } \frac{d\delta_{bc}}{dt} > 0 \\ 0, & \text{if } \frac{d\delta_{bc}}{dt} \leq 0 \end{cases} \right) \mathbf{n}_{bc} \\ - |T_{f,x}| \frac{n_{t,y}(t)}{r_h} \\ - |T_{f,x}| \frac{n_{t,z}(t)}{r_h} \end{pmatrix}. \quad (13)$$

Here $f_{f,x}$, $f_{f,y}$, and $f_{f,z}$ are the fretting force components along x -, y -, and z -axis of the robot, respectively. Further, $T_{f,x}$ is the fretting torque exerted on the robot with respect to x -axis, and is given by

$$\begin{pmatrix} T_{f,x} \\ T_{f,y} \\ T_{f,z} \end{pmatrix} = \begin{pmatrix} -\text{sgn}(\Omega_x) \pi r r_h \delta_{bc}^2 \\ r_{c,z} f_{f,x} - r_{c,x} f_{f,z} \\ r_{c,x} f_{f,y} - r_{c,y} f_{f,x} \end{pmatrix}, \quad (14)$$

where \mathbf{n}_{bc} is the surface normal of the blood clot. \mathbf{F}_f and \mathbf{T}_f vectors (similar to \mathbf{F}_c and \mathbf{T}_c) represent force constraints to

prevent the robot from moving beyond the point of contact. In (12), $n_{t,y}(t)$ and $n_{t,z}(t)$ are the components of the surface normal of the blood-clot contact at the rotating tip of the tail in the robot frame of reference denoting the fretting direction, whereas $n_{t,x}(t)$ is assumed to be -1 in the robot frame of reference denoting the direction of penetration into the blood clot. The surface normal components $n_{t,y}(t)$ and $n_{t,z}(t)$ of the tail are also computed as follows:

$$\begin{pmatrix} n_{t,y}(t) \\ n_{t,z}(t) \end{pmatrix} = \begin{pmatrix} -\cos\left(\frac{\pi}{2} - \arctan(r_{c,z}(t), r_{c,y}(t))\right) \\ -\sin\left(\frac{\pi}{2} - \arctan(r_{c,z}(t), r_{c,y}(t))\right) \end{pmatrix}, \quad (15)$$

where the negative sign is due to chirality. The material properties k_{bc} and b_{bc} are approximated by considering that the overall system must be over-damped to eliminate undesirable oscillations

$$k_{bc} = \frac{|\mathbf{F}_m| - |\mathbf{F}_d|}{\delta_{bc}} \quad \text{and} \quad b_{bc} = 2\chi\sqrt{m_r k_{bc}}, \quad (16)$$

where m_r is the mass of the robot, and χ denotes the damping tuning for the blood clot contact. χ is modeled by approximating the non-Newtonian behavior of the blood clot with a nonlinear velocity relation, i.e., $\chi = \chi_0 + \exp(\chi_1 \Omega_x)$, similitude to the variation of viscosity of fluids under high pressure. According to RFT, impact power of the tip of the tail increases with the square of the actuation frequency, which increases the local viscosity nonlinearly. Finally, the location of the clot is updated at each time-step using position dependent normal distribution function, $\psi(\mathbf{r})$, to simulate the material removal as follows:

$$x_{bc}(t + dt) = x_{bc}(0) + \text{sgn}(u_x) \frac{\psi(\mathbf{r})}{D_{ch}^2} \int_0^{t+dt} r_h \delta_{bc}^2 |\Omega_x| dt, \quad (17)$$

where $x_{bc}(t)$ and $x_{bc}(0)$ are the positions of the blood clot at time t and the initial position of the clot, respectively. u_x is the velocity of the robot along x -axis in its frame of reference. Further, we map the one-dimensional prediction of material removal into three-dimensional prediction based on the preliminary simulation results as the robot does not remove material from a single location (Fig. 4). In (17), $\psi(\mathbf{r})$

is a normal distribution function and is given by

$$\psi(\mathbf{r}) = \frac{1}{\sqrt{2\sigma^2\pi}} \exp\left[-\frac{\left(\frac{2r}{D_{\text{ch}}} - \eta\right)^2}{2\sigma^2}\right] \kappa, \quad (18)$$

where σ is the standard deviation and η is the location, i.e., center of the channel, where the maximum cumulative material removal is expected, and r is the radial position of the robot in the channel. κ is the weighing function, which is based on the location of the tip of the rotating tail, handling each of the four quadrants of the channel cross-section separately to obtain accurate distribution. We begin by simulating the rubbing behavior by solving the equation of motion (4), and obtain the rigid-body velocity vectors of the robot. Initially, the robot is assumed to be parallel to the longitudinal axis of the cylindrical channel and is concentric with the cross-section. Fig. 4 shows the rubbing behaviour of the robot against the blood clot. We allow the applied magnetic field of the two rotating permanent magnets to exert magnetic force and torque based on (3). This magnetic actuation is responsible for defining the swimming direction of the robot along x -axis. As one would expect, the contact between the robot and the blood clot constrains the motion of the robot along x -axis (Fig. 4(a)), and causes the robot to drift towards the wall with time, as shown in Fig. 4(b). Fig. 4(c) shows the components of the velocity of the robot during rubbing. The robot exhibits oscillatory motion along y - and z -axis, whereas the net displacement along x -axis is negligible. Our simulation also allows for the calculation of the removal rate of the blood clot based on (12), (13), (14), and (17). The removal rate is calculated at 26 frequencies of the rotating dipole fields, and maximum dissolution rate of $-0.834 \text{ mm}^3/\text{min}$ is observed at frequency of 35 Hz. We attribute the existence of an optimal rubbing frequency before the step-out frequency of the robot to the presence of flow against the motion of the robot and the increased damping during rubbing at relatively high frequencies.

III. IN VITRO VALIDATION OF RUBBING AGAINST BLOOD CLOTS

The dissolution and removal of blood clots are experimentally investigated using two distinct groups, i.e., dissolution using full dose of streptokinase (Group 1) and mechanical rubbing (Group 2). In each trail, the clots are prepared and inserted into catheter segments. Venous blood is drawn from two donors (male 26 years and female 24 years) into a vacutainer without anticoagulant. *Local Institutional Ethical Board approval is obtained for the preparation protocol of the blood clots, and donors gave written informed consent.* Blood clots are prepared based on the well-known protocol proposed by Hoffmann and Gill [34], with length and diameter of 7.5 mm and 4 mm, respectively. The ultimate tensile strength of the clots is approximately $1 \times 10^3 \text{ Pa}$. The clots are contained inside segments that are mounted between two rotating permanent magnets to exert magnetic torque on the dipole of the helical robot. The robots are fabricated using an aluminum spring (length, diameter, and pitch of 2.2 mm, 346 μm , and 580 μm , respectively). This spring is

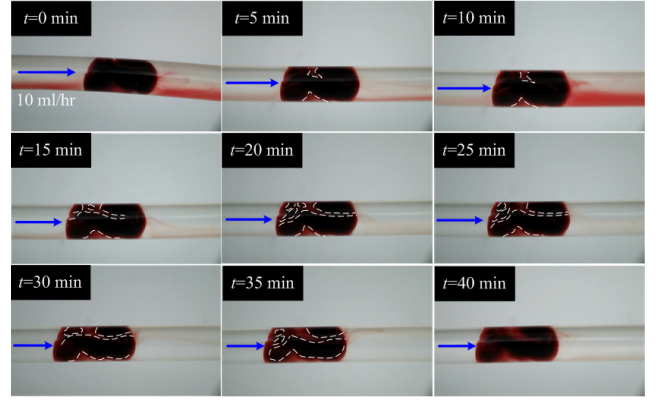


Fig. 5. A representative experiment of dissolution of a blood clot using full dose of streptokinase (1,500,000 I.U.) at flow rate, $\mathbf{U}_{\text{ch}} = [10 \ 0 \ 0]^T \text{ ml/hr}$. The blue arrow indicates the direction of the flow. The dissolution rate of the clot is $-0.19 \text{ mm}^3/\text{min}$ in this trial. At time, $t \simeq 20$ minutes, formation of fluid channels (white dashed lines) inside the clot is observed.

attached to a cylindrical NdFeB magnet with a magnetization vector oriented perpendicular to the spring axis. It is likely that the robot will be fabricated using bio-degradable or bio-absorbable material instead of the aluminum spring used in this study. Nevertheless, our hydrodynamic model is relatively general and can be modified to study bio-degradable robots. The size of the blood clots is measured using our morphological filtering algorithm [18] throughout the dissolution or the rubbing. Initially, we measure the weight of the clot (0.11 gm) and calibrate our algorithm based on the geometry of each clot. The size of the clots is calculated off-line from the recorded video images using a camera (avA1000-120kc, Basler Area Scan Camera, Basler AG, Ahrensburg, Germany) to observe the xz -plane and a Sony XCD-X710 (Sony Corporation, Tokyo, Japan) FireWire camera to assist in constructing the volume of the blood clot [27]. All experimental trials are done in the presence of a flow rate of 10 ml/hr. This flow rate is devised based on the administration and infusion rates for adult patients (maximum blood flow rates in small arteriole, capillaries, and venule are approximately 0.25 ml/hr, 0.045 ml/hr, and 0.00324 ml/hr). For instance, 10 ml of Streptokinase is usually given intravenously in a 1-hour infusion [28]. The flow rate is controlled using a dual syringe pump (Genie Plus, GT-4201D-12, Kent Scientific, Connecticut, USA). We begin by comparing the chemical lysis using streptokinase (1,500,000 I.U.) to rubbing using the robot.

A. Group 1: Dissolution using Full Dose of Streptokinase

During the process of blood clot formation, activated platelets convert circulating prothrombin into active thrombin, which in turn activates fibrinogen into fibrin. A polymeric three-dimensional network of fibrin fibers is then formed, which represents the final step in blood coagulation. Streptokinase is an enzyme secreted by several species of *streptococci* bacteria that work by converting fibrin-bound plasminogen to plasmin, a natural fibrinolytic agent which breaks down fibrin contained in the clot leading to clot lysis.

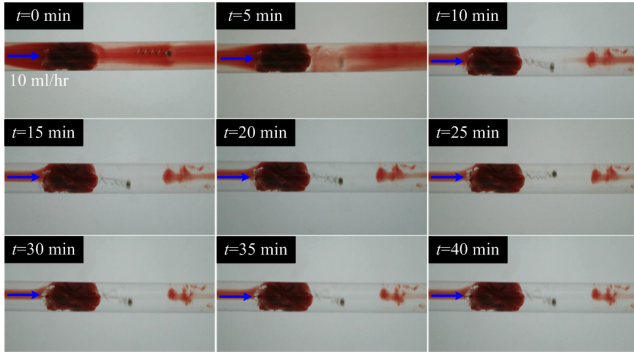


Fig. 6. A representative experiment of mechanical rubbing against a blood clot using a helical robot. The rubbing is done in the presence of flow rate, $\mathbf{U}_{\text{ch}} = [10 \ 0 \ 0]^T$ ml/hr of phosphate buffered saline. In this trial, the removal rate of the clot is $-0.885 \text{ mm}^3/\text{min}$ at frequency of 35 Hz. Please refer to the accompanying video.

In this group, the dissolution of the blood clot is achieved under the influence of streptokinase, at flow rate of 10 ml/hr, as shown in Fig. 5. The volume of the blood clot is calculated throughout a lysis period of 40 minutes. In this representative trial, the initial and final volumes are calculated to be 94.24 mm^3 and 91.99 mm^3 , respectively. The measured dissolution rate is $-0.19 \text{ mm}^3/\text{min}$. Furthermore, formation of fluid channels inside the clot is observed after approximately 20 minutes of streptokinase injection. The average dissolution rate is $-0.17 \pm 0.032 \text{ mm}^3/\text{min}$ ($n=6$).

B. Group 2: Mechanical Rubbing Against Blood Clot

Now we turn our attention to the influence of the mechanical rubbing on the removal rate of the blood clot (Fig. 6). The helical robot is propelled along x -axis towards the clot and against similar flow rate to that used in the chemical lysis experiments (10 ml/hr). Two rotating magnets (R750F, Amazing Magnets LLC, California, U.S.A) are used to actuate the robot, as shown in Fig. 2. Each permanent magnet (NdFeB) has diameter and length of 19 mm and 19 mm, respectively, with axial magnetization. The permanent magnet generates magnetic field of 0.552 T on its surface. The two permanent magnets are rotated and the linear speed of the robot is measured to be 15 mm/s, at frequency of 35 Hz. The step-out frequency of the robot is experimentally measured to be 67.3 Hz, and we observe a linear increase of the swimming speed versus the angular frequency of the rotating permanent magnets within this range. Therefore, the particular choice of the actuation frequency affects the swimming speed, i.e., the approaching speed to the blood clot, before the rubbing behaviour. The resultant magnetic field at the position of the robot is measured to be 5.5 mT. The rubbing behaviour is observed once the tip of the tail comes into contact with the clot. In the representative trial shown in Fig. 6, the initial and final volumes of the clot are calculated to be 94.24 mm^3 and 60.65 mm^3 , respectively, after 40 minutes of rubbing against the clot. The dissolution rate at frequency of 35 Hz is $-0.885 \text{ mm}^3/\text{min}$. Please refer to the accompanying video.

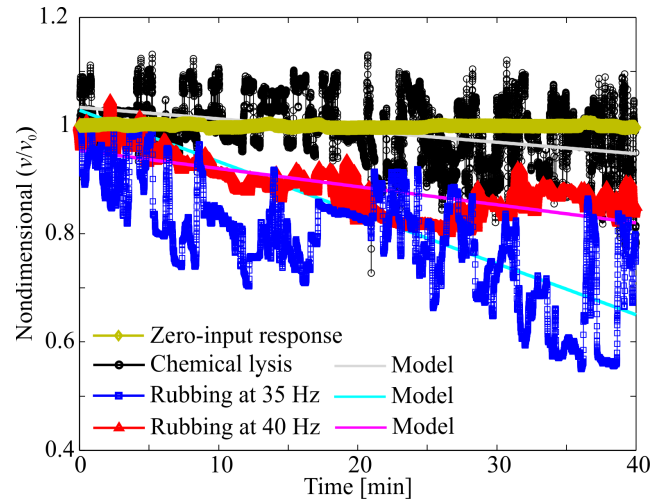


Fig. 7. Chemical lysis and mechanical rubbing of blood clots are tested on blood clot with initial volume (v_0) of 94.24 mm^3 . The zero-input response indicates that the clot does not undergo any change in its size. The lysis is done using streptokinase (1,500,000 I.U.), at flow rate of 10 ml/hr. The dissolution rate of the lysis is $-0.19 \text{ mm}^3/\text{min}$ in this trial. The rubbing is done at frequencies of 35 Hz and 40 Hz, and flow rate of 10 ml/hr. The dissolution rate of the rubbing is $-0.885 \text{ mm}^3/\text{min}$ and $-0.315 \text{ mm}^3/\text{min}$ at frequencies of 35 Hz and 40 Hz, respectively.

Mechanical rubbing achieves higher removal rate than chemical lysis, as shown in Fig. 7. The ratio between the measured volume and the initial volume (v_0/v) of the clot is measured at every time instant during the lysis and rubbing. We measure the volume ratio (v_0/v) in the absence of lysis and rubbing (zero-input response). This response shows that the clot does not undergo any change in its volume throughout the lysis or rubbing period (Fig. 7). The measured volume during lysis and rubbing exhibits noise due to the continuous chemical reaction and interaction during lysis and rubbing, respectively. Nevertheless, the lysis and rubbing have constant rates of change, as shown in Fig. 7. In contrast to chemical lysis, the removal rate of the clot can be controlled via rubbing using the frequency of the rotating dipole fields. Fig. 8 shows the influence of the rubbing frequency on the removal rate of the blood clot between 20 Hz and 45 Hz. The removal rate by the robot is almost negligible at frequencies below 20 Hz (Figs. 8(a) and (b)). Removal rates of $-0.230 \text{ mm}^3/\text{min}$, $-0.885 \text{ mm}^3/\text{min}$, and $-0.315 \text{ mm}^3/\text{min}$ are measured at rubbing frequencies of 30 Hz, 35 Hz, and 40 Hz, respectively (Figs. 8(c), (d), and (e)). Maximum removal rate is observed at frequency of 35 Hz in agreement with our simulation results. At and above rubbing frequency of 45 Hz, we observe negligible removal of the clot, as shown in Fig. 8(f).

Material removal (fretting) phenomenon is affected by at least two physical stimuli. First, the flow inside the catheter segment exerts a drag force (6) against the robot. This flow is essential to provide fair comparison between chemical lysis and mechanical rubbing. Therefore, the drag force decreases the material removal at low frequencies. Hence, the penetration depth and fretting is not effective at low frequencies, as shown in Fig. 9. Second, the non-Newtonian nature of the

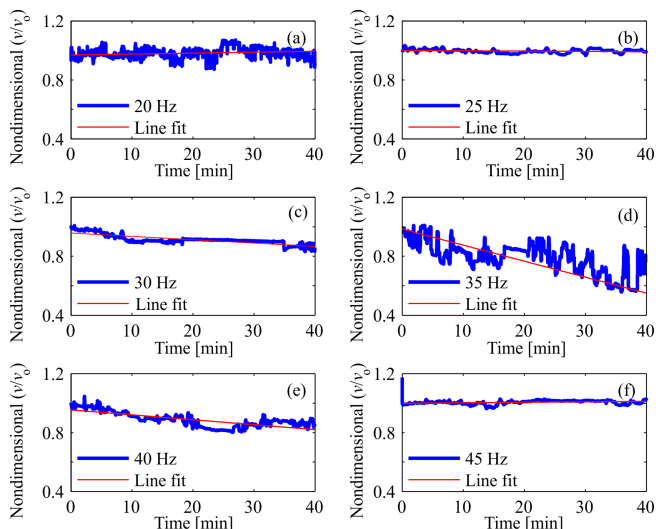


Fig. 8. The influence of rubbing frequency on the removal rate of the blood clot is investigated experimentally between 20 Hz to 45 Hz. (a and b) Mechanical rubbing is not effective below 20 Hz due to presence of flow against the helical robot. At these frequencies, the robot does not generate sufficient thrust to come into contact with the clot and achieve effective rubbing. (c, d, and e) Removal rates of $-0.230 \text{ mm}^3/\text{min}$, $-0.885 \text{ mm}^3/\text{min}$, and $-0.315 \text{ mm}^3/\text{min}$ are measured at rubbing frequencies of 30 Hz, 35 Hz, and 40 Hz, respectively. (f) The rubbing is not effective at and above frequency of 45 Hz.

blood clot affects the removal rate. Resistive force dictates that the velocity is in a linear relationship with the rotation rate, and power of the penetration increases with the square of the velocity. However, the effective viscosity of the blood clot under sudden impact should increase exponentially (or in an equivalent manner). Therefore, the damping effect becomes dominant as the frequency increases. This means that penetration decreases as spring behavior becomes more negligible. Hence, once again penetration depth and fretting becomes ineffective at high frequencies (Fig. 9).

The deviation between the theoretical and experimental removal rates is due to several aspects. First, we observe that mechanical rubbing causes small angular rotations of the clot in the direction of rubbing. Initially, the cylindrical area of the blood clot is completely in contact with the inner-surface of the segment, and hence the resulting friction force does not allow for rotation or any mobilization of the clot. However, the size of the clot decreases after rubbing for several minutes. Therefore, the contact between the clot and the inner-surface of the segment is decreased and friction is reduced. Second, the natural clot-to-clot variability in properties and original shape (during insertion of the clots inside the segments) results in a deviation between the theoretical and experimental results. The scatter in the experimental data (evident at frequencies of 30 Hz and 35 Hz) is attributed to the clot-to-clot variability. Nevertheless, the optimal rubbing frequency of the experimental removal rate is in agreement with the results of the mathematical model. The experimental results do not show significant difference within the measurement error between chemical lysis and rubbing at frequencies of 20 Hz, 25 Hz, 30 Hz, and 45 Hz.

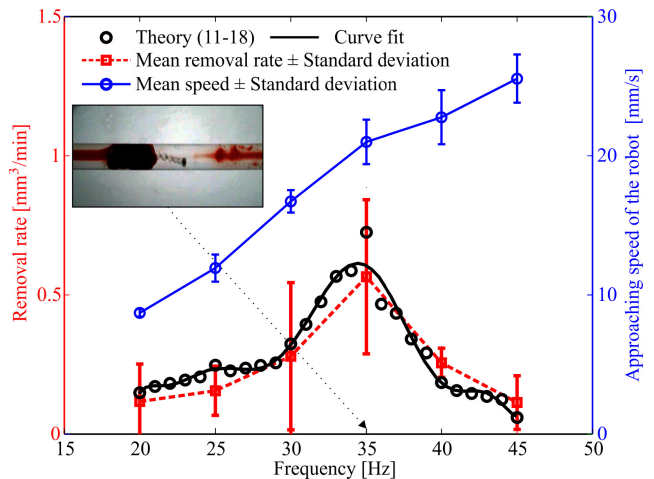


Fig. 9. The rubbing frequency influences the removal rate of the blood clot. Mechanical rubbing is effective within a frequency range of 20 Hz to 45 Hz. Maximum removal rate is achieved at 35 Hz (inset). The magnetic field at the position of the helical robot is 5.5 mT, and the flow rate is 10 ml/hr. The removal rate is calculated using (11) to (18). The approaching speed of the robot is calculated in stationary medium (phosphate buffered saline). The averages and standard deviations are calculated using 6 trials.

However, the rubbing results at 35 Hz and 40 Hz show a significant increase in the removal rate of the blood clot compared to lysis under similar conditions.

IV. CONCLUSIONS AND FUTURE WORK

We experimentally show that mechanical rubbing against blood clots using helical robots results in higher removal rates than chemical lysis using a thrombolytic agent (Table I). Streptokinase achieves dissolution rate of $-0.17 \pm 0.032 \text{ mm}^3/\text{min}$ ($n=6$), whereas rubbing achieves removal rate of $-0.56 \pm 0.27 \text{ mm}^3/\text{min}$ ($n=6$), at frequency of 35 Hz. We also investigate the influence of the rubbing frequency on the dissolution rate of the clots, and find an optimal rubbing frequency that achieves maximum removal rate at frequency of 35 Hz. Our experiments are also in agreement with the RFT-based model that describes the locomotion of the robot in low-Reynolds number and the rubbing behaviour against blood clots. The model and experimental results are valid for Reynolds numbers up to transition regimes above which hydrodynamics will drastically change due to inertial effects. This model suggests the presence of an optimal rubbing frequency that enables the robot to achieve maximum removal rate. In particular, the model predicts an optimal frequency as both low and high frequencies produce negligible removal rates. The first is ineffective owing to the excessive drag due to flow in the segment, and the second owing to the increased damping at relatively high frequencies.

As part of future studies, we will investigate the influence of mechanical rubbing with combination of full and small doses of a thrombolytic agent. Relatively small doses of a thrombolytic agent with a combination of rubbing might mitigate the side-effects of the full dose. Our permanent magnet-based actuation system will also be adapted to incorporate a medical imaging modality to localize the robot and image

TABLE I

COMPARISON BETWEEN LYSIS AND RUBBING AT 35 HZ. THE FINAL VOLUME ($v(t_f)$) IS MEASURED AFTER 40 MINUTES. THE INITIAL VOLUME (v_0) OF THE CLOT IS 94.24 MM³.

Characteristic	$v(t_f)/v_0$	Dissolution rate [mm ³ /min]
Chemical lysis	0.94±0.011	-0.17±0.032
Rubbing at 35 Hz	0.85±0.042	-0.56±0.27

the physiological environment. We also need to use biodegradable or bio-absorbable material to fabricate the helical robots. In addition, we will validate the influence of the tip geometry on the removal rate and the fretting action on the three-dimensional network of blood clots *in vivo*.

REFERENCES

- [1] J. Wang and W. Gao, "Nano/Microscale motors: biomedical opportunities and challenges," *ACS Nano*, vol. 6, no. 7, pp. 5745-5751, July 2012.
- [2] B. J. Nelson, I. K. Kaliakatsos, and J. J. Abbott, "Microrobots for minimally invasive medicine," *Annual Review of Biomedical Engineering*, vol. 12, pp. 55-85, April 2010.
- [3] J. Liu, J. Wen, Z. Zhang, H. Liu, and Y. Sun, "Voyage inside the cell: Microsystems and nanoengineering for intracellular measurement and manipulation," *Microsystems & Nanoengineering*, vol. 1, no. 15020, September 2015.
- [4] E. M. Purcell, "Life at low Reynolds number," *American Journal of Physics*, vol. 45, no. 1, pp. 3-11, June 1977.
- [5] A. Ghosh and P. Fischer, "Controlled propulsion of artificial magnetic nanostructured propellers," *Nano Letters*, vol. 9, pp. 2243-2245, June 2009.
- [6] L. Zhang, J. J. Abbott, L. Dong, B. E. Kratochvil, D. Bell, and B. J. Nelson, "Artificial bacterial flagella: Fabrication and magnetic control," *Applied Physics Letters*, vol. 94 (064107), February 2009.
- [7] A. W. Mahoney, N. D. Nelson, E. M. Parsons, and J. J. Abbott, "Non-ideal behaviors of magnetically driven screws in soft tissue", in *Proceedings of the IEEE International Conference of Robotics and Systems (IROS)*, pp. 3559-3564, Vilamoura, Algarve, October 2012.
- [8] N. D. Nelson, J. Delacenserie, and J. J. Abbott, "An empirical study of the role of magnetic, geometric, and tissue properties on the turning radius of magnetically driven screws", in *Proceedings of the IEEE International Conference on Robotics and Automation (ICRA)*, pp. 5372-5377, Karlsruhe, Germany, May 2013.
- [9] T. Xu, G. Hwang, N. Andreff, and S. Régnier, "Planar path following of 3-D steering scaled-up helical microswimmers", *IEEE Transactions on Robotics and Automation*, vol. 31, no. 1, pp. 117-127, February 2015.
- [10] Z. Lu and S. Martel, "Controlled bio-carriers based on magnetotactic bacteria," in *Proceedings of The IEEE International Conference on Solid-State Sensors, Actuators and Microsystems*, pp. 683-686, Lyon, France, June 2007.
- [11] S. Martel and M. Mohammadi, "Using a swarm of self-propelled natural microrobots in the form of flagellated bacteria to perform complex micro-assembly tasks," in *Proceedings of The IEEE International Conference on Robotics and Automation*, pp. 500-505, Alaska, USA, May 2010.
- [12] S. Sanchez, A. A. Solovev, S. Schulze, and O. G. Schmidt, "Controlled manipulation of multiple cells using catalytic microrobots," *Chemical Communications*, vol. 47, no. 2, pp. 698-700, January 2011.
- [13] W. Wang, S. Li, L. Mair, S. Ahmed, T. J. Huang, and T. E. Mallouk, "Acoustic propulsion of nanorod motors inside living cells," *Angewandte Chemie*, vol. 126, no. 12, pp. 3265-3268, February 2014.
- [14] S. K. Srivastava, M. M.-Sánchez, B. Koch, and O. G. Schmidt, "Medibots: dual-action biogenic microdaggers for single-cell surgery and drug release," *Advanced Materials*, vol. 28, no. 5, pp. 832-837, November 2015.
- [15] A. Servant, F. Qiu, M. Mazza, K. Kostarelos, and B. J. Nelson, "Controlled *in vivo* swimming of a swarm of bacteria-like micro-robotic flagella," *Advanced Materials*, vol. 27, no. 19, pp. 2981-2988, April 2015.
- [16] M. Medina-Sánchez, L. Schwarz, A. K. Meyer, F. Hebenstreit, and O. G. Schmidt, "Cellular cargo delivery: toward assisted fertilization by sperm-carrying micromotors," *Nano Letters*, vol. 16, no. 1, pp 555-561, December 2016.
- [17] F. Ullrich, F. Qiu, J. Pokki, T. Huang, S. Pane, and B. J. Nelson, "Swimming characteristics of helical microrobots in fibrous environments," in *Proceedings of the IEEE RAS/EMBS International Conference on Biomedical Robotics and Biomechatronics (BioRob)*, pp. 470-475, UTown, Singapore, June 2016.
- [18] A. Hosney, J. Abdalla, I. S. Amin, N. Hamdi, and I. S. M. Khalil, "In vitro validation of clearing clogged vessels using microrobots," in *Proceedings of the IEEE RAS/EMBS International Conference on Biomedical Robotics and Biomechatronics (BioRob)*, pp. 272-277, Singapore, June 2016.
- [19] A. Hosney, A. Klingner, S. Misra, and I. S. M. Khalil, "Propulsion and steering of helical magnetic microrobots using two synchronized rotating dipole fields in three-dimensional space," in *Proceedings of the IEEE/RSJ International Conference of Robotics and Systems (IROS)*, pp. 1988-1993, Hamburg, Germany, November 2015.
- [20] A. J. Petruska and J. J. Abbott, "Optimal permanent-magnet geometries for dipole field approximation," *IEEE Transactions on Magnetics*, vol. 49, no. 2, pp. 811-819, February 2013.
- [21] H. L. Rakotoarison, J.-P. Yonnet, and B. Delinchant, "Using coulombian approach for modeling scalar potential and magnetic field of a permanent magnet with radial polarization," *IEEE Transactions on Magnetics*, vol. 43, no. 4, pp. 1261-1264, April 2007.
- [22] C. Brennen and H. Winet, "Fluid mechanics of propulsion by cilia and flagella," *Annual Review of Fluid Mechanics*, vol. 9, pp. 339-398, January 1977.
- [23] J. J. L. Higdon and G. P. Muldowney, "Resistance functions for spherical particles, droplets, and bubbles in cylindrical tubes," *Journal of Fluid Mechanics*, vol. 298, pp. 192-210, September 1995.
- [24] A. F. Tabak and S. Yesilyurt, "Improved kinematic models for two-link helical micro/nanoswimmers," *IEEE Transactions on Robotics*, vol. 30, no. 1, pp. 14-25, February 2014.
- [25] A. J. Hanson and H. Ma, "Quaternion frame approach to streamline visualization," *IEEE Transactions on Visualization and Computer Graphics*, vol. 1, no. 2, pp. 164-174, June 1995.
- [26] A. G. Erman and A. F. Tabak, "Resistive force theory based modeling and simulation of surface contact for swimming helical micro robots with channel flow," in *Proceedings of the IEEE/ASME International Conference on Advanced Intelligent Mechatronics*, pp. 390-395, Besançon, France, July 2014.
- [27] H. Longuet-Higgins, "A computer algorithm for reconstructing a scene from two projections," *Nature*, vol. 293, no. 10, pp. 133-135, September 1981.
- [28] David A. Morrow, "Myocardial infarction: a companion to braunwald's heart disease," *Elsevier Health Sciences*, July 2016.
- [29] J. Funda, R. H. Taylor, and R. P. Paul, "On homogeneous transforms, quaternions, and computational efficiency," *IEEE Transactions on Robotics and Automation*, vol. 6, no. 3, pp. 382-388, June 1990.
- [30] N. Krasokha, W. Theisen, S. Reese, P. Mordasini, C. Brekenfeld, J. Gralla, J. Slotboom, G. Schrott, and H. Monstadt, "Mechanical properties of blood clots—a new test method", *Materials Science and Engineering Technology*, vol. 41, no. 12, pp. 1019-1024, December 2010.
- [31] T. Azar, and V. Hayward, "Estimation of the fracture toughness of soft tissue from needle insertion," in *Proceedings of the International Symposium on Computational Models for Biomedical Simulation (IS-BMS) Lecture Notes in Computer Science*, vol. 5104, Springer Verlag, pp. 166-175, July 2008.
- [32] T. Chanthasopephan, J. P. Desai, and A. C. W. Lau, "Determining fracture characteristics in scalp cutting of soft tissue," in *Proceedings of the International Conference on Biomedical Robotics and Biomechatronics (BioRob)*, pp. 283-288, Tuscany, Italy, February 2006.
- [33] I. Ionescu, J. E. Guilkey, M. Berzins, R. M. Kirby, and J. A. Weiss, "Simulation of soft tissue failure using the material point method," *Journal of Biomechanical Engineering*, vol. 128, pp. 917-924, December 2006.
- [34] A. Hoffmann and H. Gill, "Diastolic timed vibro-percussion at 50 Hz delivered across a chest wall sized meat barrier enhances clot dissolution and remotely administered streptokinase effectiveness in an in-vitro model of acute coronary thrombosis", *Thrombosis Journal*, vol. 10, no. 23, pp. 1-16, November 2012.